Research Article

Optimization of process parameter of FS-welding of aluminum-lithium alloy (AA8090) by using desirability analysis

Munna Singh Dahiya*,a, Meenu Guptab

Department of Mechanical Engineering, National Institute of Technology, Kurukshetra, India

Article Info	Abstract
	This study explores the potential of Friction Stir Welding (FSW) for Aluminum Lithium (AA8090) Alloys, emphasizing the crucial role of experimental investigations in optimizing the FSW process. Using a vertical machine center (VMC) with a customized fixture and tool for FSW, factors like Rotational speed (RS), Tilt angle (TA), and Welding Speed (WS) are considered to enhance ultimate tensile strength (UTS) and % elongation (EL). A regression model based on Response Surface Methodology's Central Composite Design (CCD) is used to analyze UTS and % EL. The effectiveness of welded joints is comparable to the parent metal, with optimal UTS and EL achieved at 1428 rpm rotational speed, 36.4 mm/min welding speed, and 1.5° tilt angle. While significant interaction effects are observed in UTS, none are noted in EL. FSW joint performance is evaluated through microstructural analysis, microhardness distribution and fractography analysis.

1. Introduction

FS-welding is a solid-state joining procedure that has received considerable interest in recent years due to its several advantages over traditional welding techniques, such as increased joint strength, decreased distortion and reduced thermal distortion. In a variety of industries, notably aerospace, automobile, marine and defence the method has been used successfully to combine diverse materials, particularly aluminium alloys. With the continuous development of new materials, it is essential to investigate the feasibility and performance of FS-welding for emerging alloys, such as Aluminum Lithium (AA8090) alloys [1]. The fundamental concept of FSW technique is depicted in Figure 1. It consists of a non-consumable rotating tool having a specially designed tool pin and shoulder. Tool pin is plunged into the faying faces of sheets or plates to be joined thus tool moves in the transverse direction along the length. The purpose of this study is to investigate the viability of friction stir welding (FS-welding) of AA8090 Aluminum Lithium alloy and to conduct a comprehensive experimental investigation of the process parameters, microstructural characterization and mechanical properties of the resulting joints. Utilizing the CCD technique of Surface Methodology (RSM), regression design models for UTS and % elongation (EL) of welded joints are developed [2-7]. In addition, microstructural analysis, microhardness distribution and fractography are performed to evaluate the performance of the FS-welding joints and comprehend the links between the process parameters, microstructure and mechanical properties [8-10].

The experimental setup involves using a vertical machine center (VMC) equipped with a custom fixture and tool specifically designed for the FS-welding process [11-12]. During the FS-welding process, the VMC is combined with a control system that manages the RS,

WS and axial force providing accurate and reproducible outcomes. The precise design of the experimental procedure ensures a stable and evidenced for the FS-welding procedure, which contributes to the dependability and reproducibility of the obtained results.
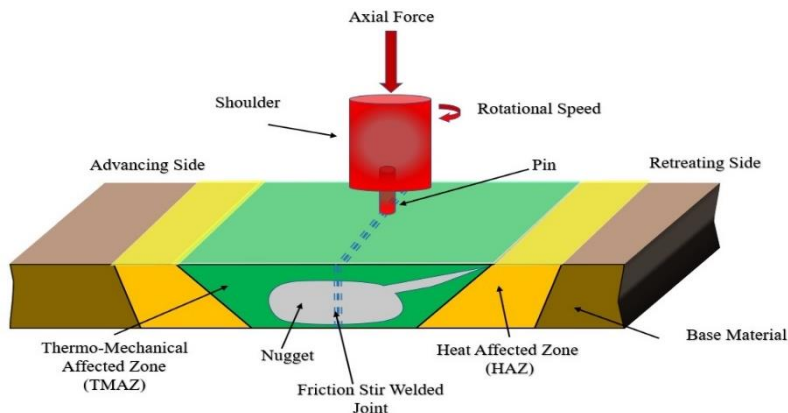

Fig. 1. FS-welding with its components

The outcome of the study discusses the results and focusing on the parametric optimization, microstructural analysis, microhardness distribution, and fractography of the FS-welding joints. Finally, the last part conclusion summarizes the study's conclusions and highlights the implications of the findings for the improvement of FS-welding processes and the potential applications of AA8090 Aluminum Lithium alloys in various industries. Mahto et al. conducted a study to determine the physical parameters of AA 6061-T6 Al-alloy and AISI 304 stainless steel friction stir lap welded joints. The study discovered that faster tool speeds and slower WS led to stronger joints [13]. Verma and Misra studied the FS-welding of dissimilar Al-alloys and found that joint strength is maximized when a stronger Al-alloy is utilized to cover the AS [14]. Verma et al. investigated the temperature distribution during FS-welding of Al-6082 plates using eight L-shaped thermocouples[15]. Verma et al. FS-welding of Al-Mg-Si-Mn alloy (AA6082) for butt joint fabrication[16], while Verma et al. evaluated six different tool pin-geometries for FS-welding of aviation-grade Al-alloy (AA6082) [17]. Verma et al. studied the effects of preheating and water cooling on the properties of friction-stir-welded AA6082 joints[18], and Verma et al. studied FS-welding of aviation grade Al-alloy[19]. Additionally, Verma et al. used a modified vertical milling machine to perform FS-welding on AA7039 plates [20], while Mahto et al. investigated mechanical factors such as ultimate UTS and fractography and the influence of welding and rotating speeds[21]. Raja et al. examined the effect of FS-welding on the microstructure and physical parameters of two Al-alloys with variable hardness levels: AA7475-T651 and AA2219-O.ls [22]. Rajendran et al. investigated the effect of tool TA on the strength of friction stir lap welding of AA2014-T6 Al-alloy[23], while Rajkumar et al. optimized the FS-welding process for dissimilar Al-alloys AA 5052 and AA 6061[24]. Lastly, Mehta and Badheka conducted two studies; one in 2016 [25] to investigate defect development in FS-welding using different tool pin designs and another in 2017 [26] to investigate the dissimilar FS-welding of copper and Al- using nine different tool designs. Overall, these experimental studies prove the potential of FS-welding and highlight the importance of varying process parameters to optimize FS-welding for varied materials and applications. Several studies have used artificial intelligence (AI) techniques, specifically artificial neural networks (ANN) to perfect the FS-welding process and predict the resulting joint properties. Boldsaikhan et al. [27] evaluated the quality of FS-welding in real-time using feedback signals, achieving high accuracy rates for identifying welds

with defects and classifying weld strength. Fratini et al. [28] used an artificial neural network with a finite element design model to forecast the average grain size of FS-welding joints. Both Ghetiya and Patel were present [29] optimized the FS-welding process parameters for an aluminum alloy using an ANN to predict the joint's tensile strength based on input parameters. Wakchaure et al. [30] used Taguchi-based Grey Relational Analysis and ANN to optimize FS-welding parameters, while Alkayem et al. [31] ANN design models were created to predict weld quality based on process characteristics. Kamal Babu et al. [32] ANN and algorithm (GA) techniques were used to optimize FS-welding of cryorolled AA2219 alloy for a defect-free weld junction with optimal strength. Additionally, Masoudi Nejad et al. [33]AA2024-T351's fracture behaviour and fatigue crack propagation rate were explored utilizing ANN to predict the ensuing attributes. Prasanna et al. (2013)[34]examined the impact of heat-treatment techniques and tool pin geometries on FS-welding of AA6061, comparing the mechanical behavior of single-pass and double-pass welded joints. These studies prove the potential of AI techniques to optimize FS-welding and predict resulting joint properties, leading to enhanced quality and cost-effective production. V. Haribalaji et al. perfected the FS-welding process parameters to join dissimilar AA2014 and AA7075 aluminum alloys using the RSM and Taguchi methods. Author found that the WS had a significant influence on the joint strength of the welded alloys [35]. A. Nait Salah et al. perfected the process parameters of FS-welding joints of dissimilar aluminum alloys AA3003 and AA6061 using the RSM. Author found that the RS and WS had a significant effect on the mechanical properties of the welded joints [36]. Sarvaiya and D. Singh proposed a particle swarm optimization algorithm to select the best process parameters in FS-welding/processing. Author found that the proposed algorithm provided a more efficient and accurate optimization process for the selection of the optimal process parameters[37]. M. Simoncini et al. performed an experimental and numerical investigation on forming limit curves of AA6082 aluminum alloy at high strain rates. Author concluded that the forming limit curves of the AA6082 aluminum alloy were significantly influenced by the strain rate[38]. Abd Elnabi et al. investigated the influence of FS-welding parameters on metallurgical and mechanical properties of dissimilar AA5454-AA7075 aluminum alloys. Author concluded that optimizing the FS-welding parameters led to improved mechanical properties and a more refined microstructure[39]. Subramanian et al. used RSM to optimize FS-welding process parameters for dissimilar magnesium alloys. The study showed that optimized parameters significantly improved the weld quality, mechanical properties, and microstructure[40]. Khan) optimized FS-welding of AA6062-T6 alloy, showing that proper selection of process parameters can enhance the mechanical properties of the joint[41]. Haribalaji et al. optimized FS-welding process parameters for joining dissimilar AA2014 and AA7075 aluminum alloys. Author found that optimizing the parameters improved the tensile strength and microstructural characteristics of the joint [42]. The alloys exhibit high strength-to-weight ratios, excellent fatigue properties and reduced density making them suitable for various applications requiring lightweight and high-performance materials. The purpose of this investigation focuses on the benefits of friction stir welding (FS-welding) over conventional welding techniques and stresses the significance of experimental research in enhancing the FS-welding process and the resulting joints.

2. Materials and Methods

2.1. Material

The material used for this study is AA8090 having welding plate's dimensions of 100 mm x 70 mm x 6 mm. Table 1 provides details on the chemical composition and mechanical properties of AA8090.

Table 1. Chemical Composition and mechanical properties of AA8090

Elements	Mg	Si	Li	Zr	Fe	Cu	Zn	Ti	Al
Percentage	0.95	0.20	2.30	0.12	0.33	1.3	0.25	0.10	Bal

Density	Young's Modulus	Poisson's Ratio	Tensile Strength	% Elongation	Hardness (HV)	Shear Strength
2.54 g/cc	77 GPa	0.3	450Mpa	7	158	270Mpa

2.2. Experimental Setup

The present study involves the use of a vertical machine center (VMC) to conduct the FS-welding process and Specifications of Vertical Milling Center (VMC) shown in Table 2. A fixture and tool are specifically designed for this purpose, as shown in Figure 2.

SD = 18mm

PL = 5.80mm

PD = 6mm

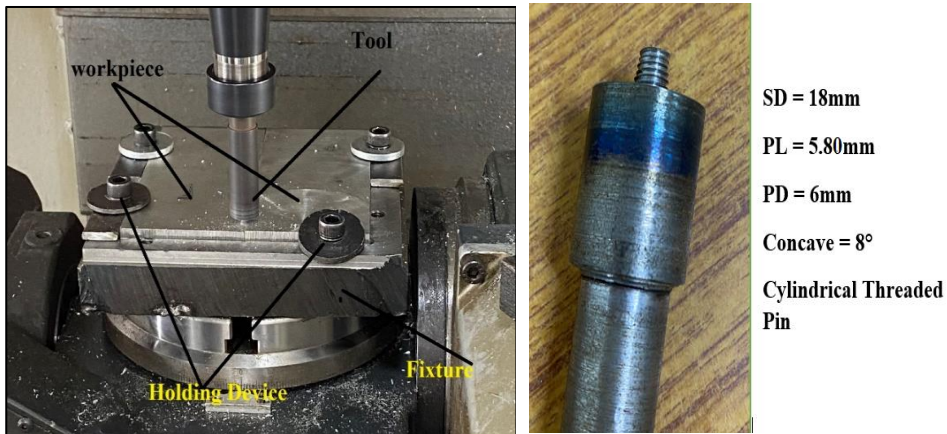Concave = 8°

Cylindrical Threaded Pin

Fig. 2. Fixture and tool used in the FS-welding process

The fixture is designed to firmly hold the workpiece during the FS-welding process, while the tool generates the necessary heat to melt the material and join the workpiece. The tool is mounted on the spindle of the VMC, while the fixture is attached with bed of machine. The VMC is equipped with a control system to regulate the RS, WS and TA applied during the FS-welding process.

Table 2. Specifications of vertical milling center (VMC)

Specifications	Values
Company	MAXMILL++(Vertical Milling Center)
Control system	Siemens 828D
Rpm range	100-8000rpm
Motor capacity	7kw
Programmable feed rate	0-10m/min
X-Axis Travel(Longitudinal Travel)	600mm
Y-Axis Travel(Latitudinal Travel)	450mm
Z-Axis Travel(Vertical Travel)	500mm

2.3. Experiment Design and Procedure

This study uses the design of experiment (DOE) approach, specifically response surface methodology (RSM) to optimize FS-welding process parameters. RSM is a mathematical practice introduced by Box and Wilson in 1951, used to analyze and optimize processes. It is particularly useful when multiple variables significantly influence the process's outcomes. Using RSM, the relationship between input variables and outcomes can be expressed, and an experimental matrix can be designed to determine optimal conditions.
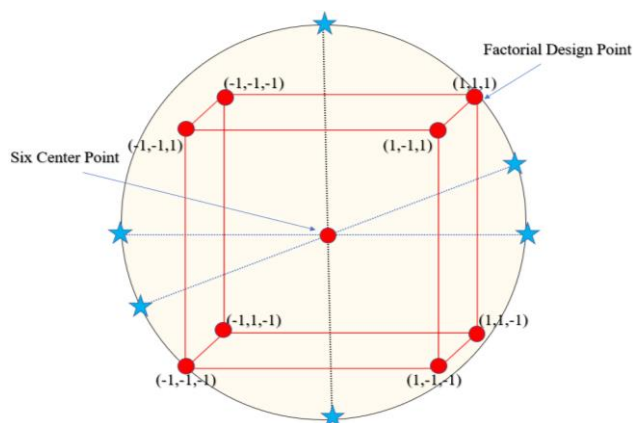

Fig. 3. Design point in CCD

To address the curvature in the response surface, the study adopts a second-order design model with interaction effects. As an economical and precise design technique, central composite design (CCD) is adopted. The experimental matrix is made up of factorial design, star and centre points as well as process variables with varying values of RS, WS and TA. The CCD design is made up of three groups of design points, as shown in Table 3. The CCD approach was used to design a total of 20 tests. Table 5 shows the experimental parameters and matching responses for all 20 studies.

Table 3. Input variables and their values

Symbol	Input Parameter	Units	Level		
			Low	Medium	High
A	RS	rpm	1428	1652	1876
B	WS	mm/min	24.6	36.4	48.2
C	TA	degree	1.1°	1.5°	1.9°

Table 4. Detail of CCD design group

No. of Input Variables (k)	Factorial Points (2k)	Star Points (2k)	Center Points (N)	Total
3	8	6	6	20

Numerous researchers have used a variety of experimental design methods to generate regression equations, but central composite rotatable design (CCD) is regarded as one of the most efficient and accurate design methods. As illustrated in Figure 3, the design incorporates three sets of points, namely factorial design, star, and centre points. As indicated in Table 4, the experiment incorporates three process variables: RS, WS and TA, each with three distinct levels.[2], [4].

Table 5. Experimental design and its results

Exp no.	Coded welding parameters			Value of welded parameters			UTS (MPa)	% Elong. (%)
	RS (rpm) A	WS (mm/min) B	Tilt angle (°)C	RS (rpm) A	WS (mm/min) B	Tilt angle (°)C		
1	-1	1	-1	1428	48.2	1.1	356	7.46
2	0	0	0	1652	36.4	1.5	360	7.23
3	0	-1	0	1652	24.6	1.5	328	5.53
4	1	-1	-1	1876	24.6	1.1	233	3.41
5	0	0	1	1652	36.4	1.9	341	6.73
6	0	0	0	1652	36.4	1.5	371	7.54
7	0	0	0	1652	36.4	1.5	362	6.97
8	1	1	-1	1876	48.2	1.1	316	5.21
9	-1	1	1	1428	48.2	1.9	349	6.88
10	-1	-1	1	1428	24.6	1.9	359	7.31
11	1	1	1	1876	48.2	1.9	333	5.87
12	0	1	0	1652	48.2	1.5	340	6.17
13	1	-1	1	1876	24.6	1.9	281	4.89
14	0	0	-1	1652	36.4	1.1	306	5.79
15	-1	0	0	1428	36.4	1.5	407	8.13
16	0	0	0	1652	36.4	1.5	354	7.27
17	1	0	0	1876	36.4	1.5	343	6.61
18	0	0	0	1652	36.4	1.5	352	7.03
19	0	0	0	1652	36.4	1.5	350	7.05
20	-1	-1	-1	1428	24.6	1.1	353	6.91

2.4. Testing

For the current investigation, rectangular strips of 100×12×6 mm was cut from of the welded sample to use a power hacksaw in order to perform UTS and microhardness testing. Using an end milling on a milling machine, these strips were subsequently turned into tensile specimens in accordance with ASTM E8M-04 and with the orientation of the specimens opposite to the welding direction. Utilizing a servo-controlled universal testing machine, the ultimate tensile and EL of the friction stir-welded joint were measured by UTM (universal testing machine). Figure 4 is a pictorial view of the tensile specimens utilised in the research work.

In this study, rectangular strips measuring 25 mm × 5 mm × 6 mm were cut from the welded plates to prepare the specimens for microstructure analysis. To ensure the surfaces of the specimens were uniform, emery papers with varying grit sizes were used ranging from 200 to 2000. The surfaces were then cloth-polished to make them scratch-free and reflective. Chemical etching with Kroll's reagent was applied to reveal the microstructure and an optical microscope (Conation Technologies) was used to observe and analyze the different welding zones. Figure 5 describes a photographic view of the metallurgical samples. The microstructure analysis is a crucial step for understanding the properties of the welded joint, as it provides essential information about the grain structure, phase composition and other significant characteristics of the material.
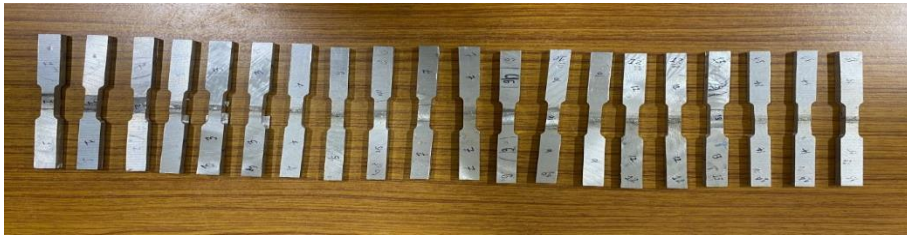
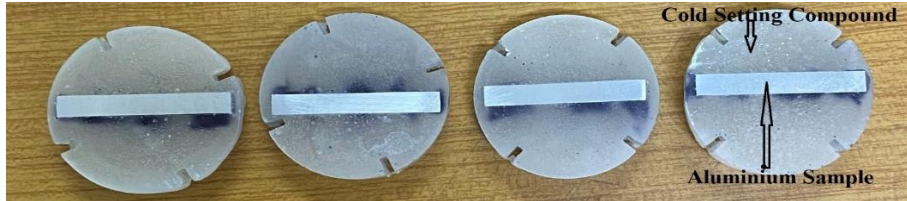Fig. 4. Photographic representation of tensile specimens

Fig. 5.Photographic depiction of (microstructure and microhardness) samples

The use of emery papers and cloth polishing helps to ensure that the surfaces of the specimens are free from scratches and other surface defects that may affect the accuracy of the analysis. The optical microscope and Kroll's reagent provide a powerful combination of tools for visualizing and analyzing the microstructure of the material.
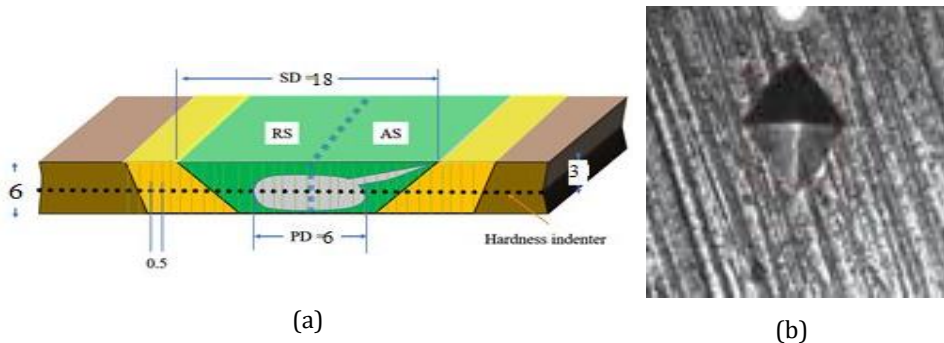

(a)

(b)

Fig. 6. The impression of the indenter on the surface of the specimen (a) Schematics diagram of different location for measuring microhardness and (b)Impression indentation

Microhardness testing is a vital method for assessing the mechanical properties and hardness of materials particularly at small scales. The precise Vickers indenter allows accurate measurements providing insights into strength, toughness and other critical properties. Proper sample preparation is crucial to obtain reliable results, as surface defects can affect microhardness measurements. In this study, rectangular strips measuring 25 mm × 5 mm × 6 mm cut from welded plates and prepared with emery sheets of differing grits. Cloth-polishing ensured reflective and scratch-free surfaces. A Vickers microhardness tester analyzed the specimens at a 100 g load yielding precise microhardness measurements. Figures 6(a) and (b) depict the indenter imprint and microhardness distribution points, respectively.

3. Experimental Result and Analysis

The sufficiency test is essential for ensuring the precision and dependability of the design model system. Variables such as sum of the squares (SS), lack-of-fit test and design model descriptive statistic can be used to evaluate the design model's fit. These testing and evaluations are simplified by statistical software.

Table 6. ANOVA for UTS

Independent variable	SS	df	MS	F-value	P-value	
Model (Prototype)	23836.86	9	2648.54	39.69	< 0.0001	Significant
A-RS	10112.40	1	10112.40	151.53	< 0.0001	
B-WS	1960.00	1	1960.00	29.37	0.0003	
C-TA	980.10	1	980.10	14.69	0.0033	
AB	2520.50	1	2520.50	37.77	0.0001	
AC	544.50	1	544.50	8.16	0.0171	
BC	242.00	1	242.00	3.63	0.0860	
A^2	1007.05	1	1007.05	15.09	0.0030	
B^2	1314.55	1	1314.55	19.70	0.0013	
C^2	2880.36	1	2880.36	43.16	< 0.0001	
Residual	667.34	10	66.73			
Lack of Fit	362.50	5	72.50	1.19	0.4269	not significant
Residual error	304.83	5	60.97			
Cor Total	24504.20	19				

Table 7. ANOVA for % elongation

Independent variable	SS	df	MS	F-value	P-value	
Model (Prototype)	22.49	9	2.50	28.22	< 0.0001	significant
A-RS	11.45	1	11.45	129.26	< 0.0001	
B-WS	1.25	1	1.25	14.15	0.0037	
C-TA	0.8410	1	0.8410	9.49	0.0116	
AB	0.8844	1	0.8844	9.99	0.0102	
AC	0.6728	1	0.6728	7.60	0.0203	
BC	0.4050	1	0.4050	4.57	0.0582	
A^2	0.7064	1	0.7064	7.97	0.0180	
B^2	2.82	1	2.82	31.87	0.0002	
C^2	1.00	1	1.00	11.30	0.0072	
Residual	0.8858	10	0.0886			
Lack of Fit	0.6621	5	0.1324	2.96	0.1294	not significant
Residual error	0.2237	5	0.0447			
Cor Total	23.38	19				

In this study, Design-Expert software was used to analyze experimental outcomes and assess design model adequacy. Sum of squares, lack-of-fit test and design model summary statistics were considered. Results indicate that the quadratic design model is suitable for both UTS and EL. Insignificant terms were identified and removed through backward elimination to enhance design model adequacy. Pooled ANOVA results after elimination

are presented in Tables 8 and 9 for UTS and EL, respectively. The adequacy check confirms the design model's suitability for predicting responses across different input parameter combinations.

Table 8. Pooled ANOVA for UTS

Independent variable	SS	df	MS	F-value	P-value		% Contribution
Model (Prototype)	23594.86	8	2949.36	35.68	< 0.0001	significant	
A-RS	10112.40	1	10112.40	122.33	< 0.0001		42.85
B-WS	1960.00	1	1960.00	23.71	0.0005		8.30
C-TA	980.10	1	980.10	11.86	0.0055		4.15
AB	2520.50	1	2520.50	30.49	0.0002		10.68
AC	544.50	1	544.50	6.59	0.0262		2.30
A^2	1007.05	1	1007.05	12.18	0.0051		4.26
B^2	1314.55	1	1314.55	15.90	0.0021		5.57
C^2	2880.36	1	2880.36	34.84	0.0001		12.20
Residual	909.34	11	82.67				3.80
Lack of Fit	604.50	6	100.75	1.65	0.2990	not significant	2.56
Residual error	304.83	5	60.97				1.29
CorTotal	24504.20	19					

Table 9. Pooled ANOVA for % elongation

Independent variable	SS	df	MS	F-value	P-value		% Contribution
Model (Prototype)	22.09	8	2.76	23.53	< 0.0001	significant	
A-RS	11.45	1	11.45	97.57	< 0.0001		51.83
B-WS	1.25	1	1.25	10.68	0.0075		5.65
C-TA	0.8410	1	0.8410	7.17	0.0215		3.80
AB	0.8844	1	0.8844	7.54	0.0190		4.00
AC	0.6728	1	0.6728	5.73	0.0356		3.04
A^2	0.7064	1	0.7064	6.02	0.0320		3.19
B^2	2.82	1	2.82	24.06	0.0005		12.76
C^2	1.00	1	1.00	8.53	0.0139		4.52
Residual	1.29	11	0.1173				5.63
Lack of Fit	1.07	6	0.1778	3.98	0.0757	not significant	4.85
Residual error	0.2237	5	0.0447				1.01
Cor Total	23.38	19					

Table 10. Fit statistics data for UTS, and % elongation

	S.D.	Mean	CV (%)	R^2	Adjusted R^2	Predicted R^2	Adeq. Precision
UTS	9.09	339.70	2.68	0.9629	0.9359	0.8159	27.4999
EL	0.3426	6.50	5.27	0.9448	0.9046	0.7125	21.8585

By dividing the mean square value for the design models by the mean square values of the residuals, the F- value of the design model is calculated. The F- value test is used to look at the relationship between the residual variance and the variance in the design model. The percentage will be close to one if the variances are almost equal, suggesting that the model of design may not have a big impact on the outcomes. The developed design models for UTS and % elongation (EL) have F-values of 35.68 and 23.53%, each with a P-value of less than 0.01. The developed design model has a substantial impact on the outcomes if the Prob > F value is below 0.05, which is the degree of confidence used in this study to determine whether the design model is adequate. The most important terms in the design model for UTS are A, B, C, AB, AC, A^2, B^2 and C^2, whereas the most important terms in the design model for EL are A, B, C, AB, AC, A^2, B^2 and C^2. By dividing each term's sum of square by the sum of squares for the design model, the proportional contribution made by each design modeling term is determined.
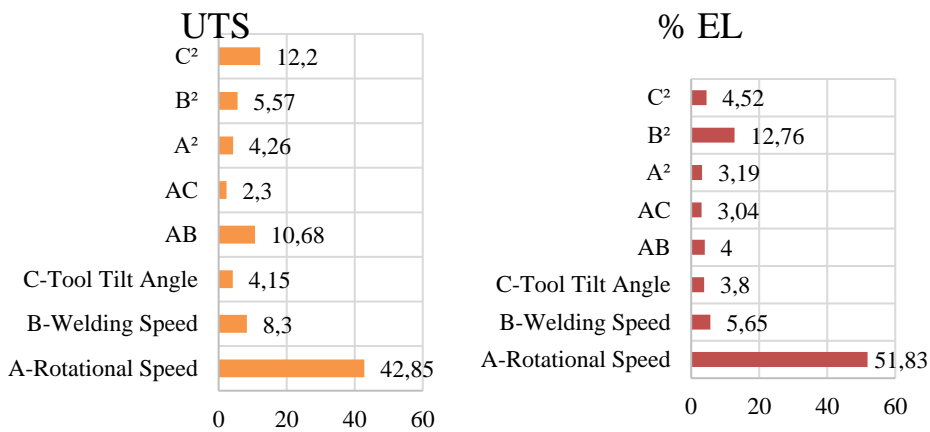
Fig. 7. Contributions of various significant terms for both design models

The contributions of different important variables for both design models are shown in Figure 7 which reveals that RS provides 42.85% for UTS and 51.83% for EL. The design model component is not significant if the p-value is higher than 0.05. According to Tables 8 and 9 the lack of fit F-value for UTS and EL are 1.65 and 3.98, accordingly, indicating a negligible joint with pure error. Noise may be to blame for the lack of fit probability for UTS and EL which are 0.2990 and 0.0757, respectively. The designed models are suitable due to this negligible lack of fit. According to Table 10 the determination coefficients (R^2) for UTS and EL are 96.29% and 94.48%, respectively. A closer fit between the response designing model and the experimental data is shown by higher R^2 values. Less fluctuation between experimental and predicted outcomes can be seen in R^2 values that are closer to 1. R^2 values alone however, should not be taken into account as sufficient for the suitability of the established design model. Therefore, other properties such as for design model adequacy, adjusted R^2, predicted R^2 and adequate precision are also taken into account. Both the predicted R^2 (71.25) and adjusted R^2 (90.46%) for EL and the predicted R^2 (81.59%) and adjusted R^2 (93.59%) for UTS show a high degree of agreement. A signal-to-noise ratio (S/N) value greater than 4 is typically needed to achieve adequate precision.

For UTS and % elongation (EL), the appropriate precision values in this investigation were found to be 27.49 and 21.85, respectively. The generated design models can be used to direct the design space and forecast values for both responses thanks to these high values, which imply adequate signal strength. Both design models' R^2 and adequate precision values highlight how important they are for fitting and forecasting experimental data.
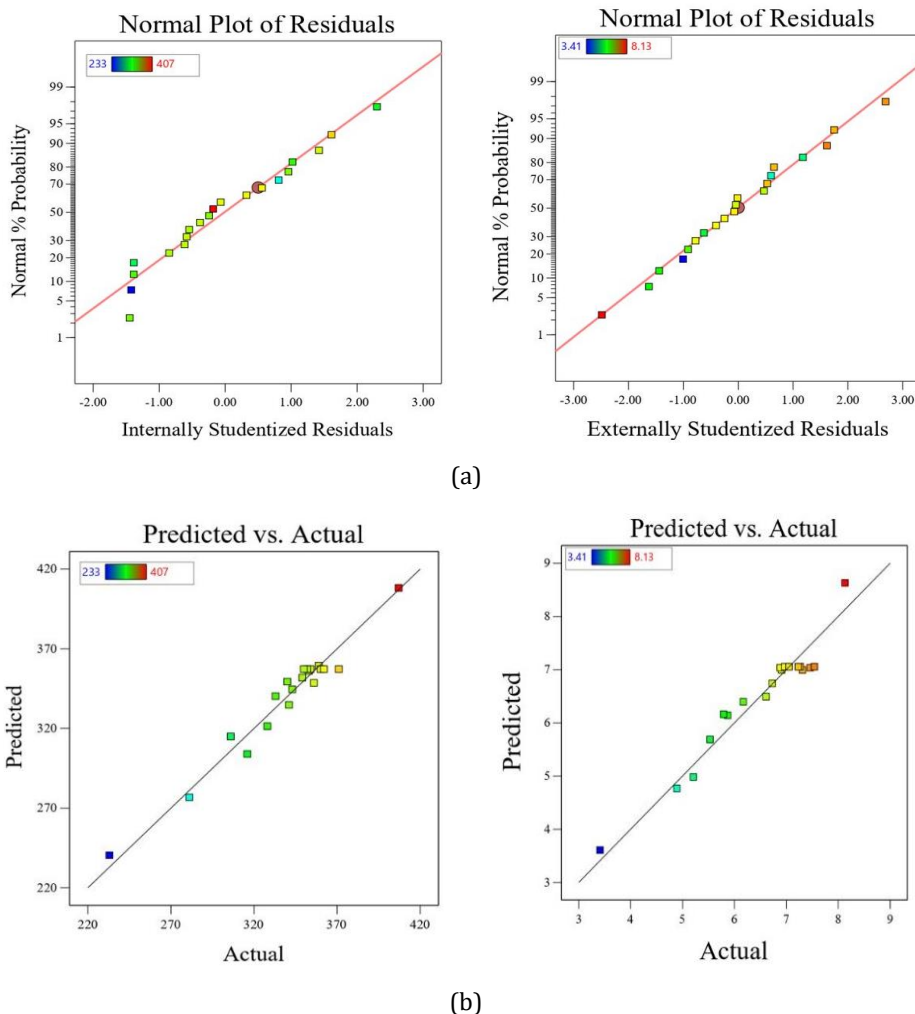
(a)

(b)

Fig. 8. Diagnostics plots of UTS and EL (a) normal probability curve (b) predicted vs. actual

$$UTS = +1521.11387 - 1.78461A + 1.52384B + 479.4588C + 0.00671AB + 0.092076AC + 0.000381A^2 - 0.157021B^2 - 202.27273C^2 \tag{1}$$

$$EL = +37.79353 - 0.047584A + 0.351918B + 6.68778C + 0.000126AB + 0.003237AC + 0.000010A^2 - 0.007277B^2 - 3.76989C^2 \tag{2}$$

The normal probability curve for residuals is shown in Figure 8(a), and it shows that for both UTS and EL, residuals are aligned with a straight line and fall within 3 limits. Figure 8(b) shows that for UTS and EL, the predicted values from the design model agree with the experimental values, supporting the validity of the findings from the ANOVA tables. Figures 8 meet the requirements for error normalcy and predictive potential. The regression designs for UTS and EL are shown in equations (1) and (2), respectively.

3.1. Effect of Welding Parameters on UTS

A regression analysis model for UTS is presented in this paper emphasizing the importance of first- and second-order variables as well as the relationship between the tools RS and TA. These terms are significant in the following order: A, B, C, AB, AC, A^2, B^2, and C^2. Variations in joint characteristics occur throughout the FS-welding process due to temperature cycles, cooling speeds and plastic deformation. These modifications also have an impact on the creation, growth, and dissolution of reinforcing precipitates in the NZ.

(a)

(b)

(c)
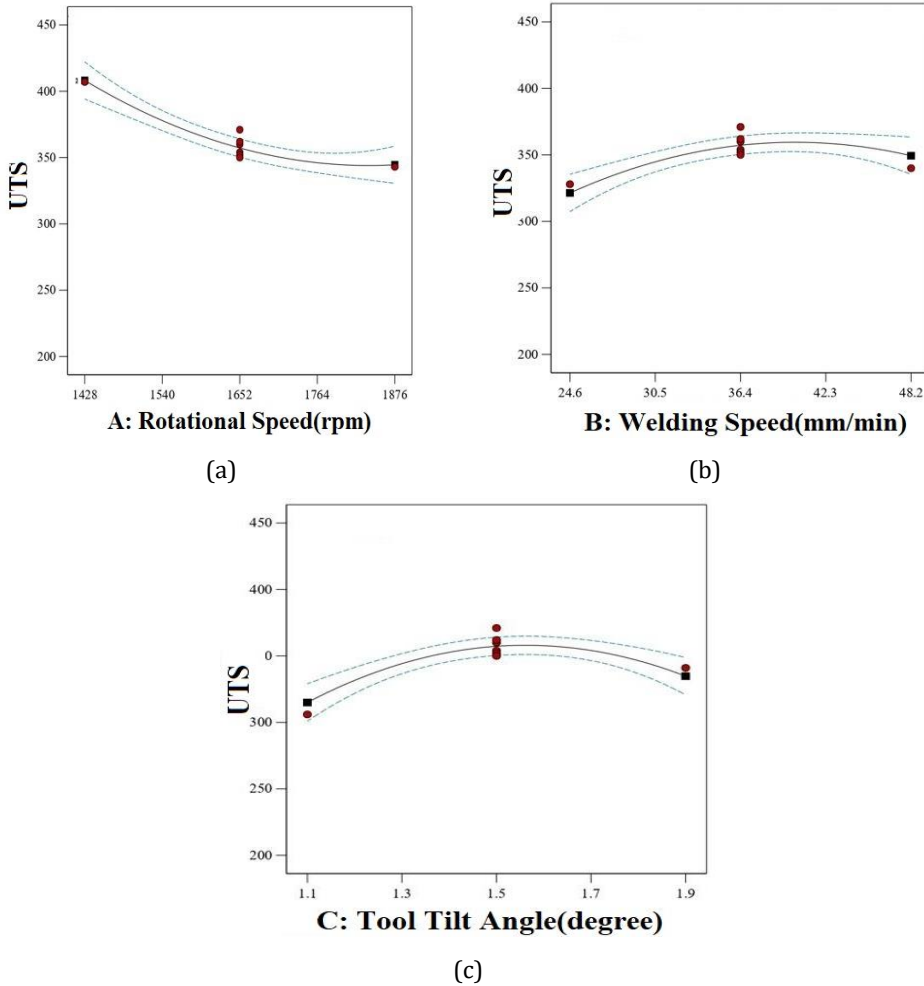
Fig. 9. Performance of overall factors in UTS (a) rotation speed vs UTS, (b) WS vs UTS and (c) tool TA vs UTS

These precipitates dissolve in Aluminium Lithium (AA8090) Alloys during FS-welding mechanical stirring, but the HAZ has a coarser structure. In order to regulate the degree of coarsening, which is controlled by the rate of cooling and thermal cycles throughout the FS-welding process, proper control of temperature is essential.

The Figure 9 highlights the individual effects of process parameters on UTS. Figure 9 (a) describes that UTS decreases significantly when RS increases from 1428 rpm to 1876 rpm. This phenomenon observed by other researchers in precipitation-hardening alloys can be

attributed to the increased heat input resulting from the higher RS [23]. The subsequent turbulence in the NZ causes material to rise to the workpiece's upper surface as flashes, which then creates tunnel defects in the NZ. Out of the 20 experiments conducted in the study only two joint presented tunnel defects all of which were fabricated at the higher RS of 1876 rpm. The tunnel defects contributed to a reduced tensile strength[43], [44]. Figure 9 (b) describes the relationship between WS and UTS showing a minimum UTS at lower WS a sharp increase up to a WS of 36.4 mm/min and a subsequent decline as WS continues to increase.

3.2. Interaction Effects on UTS

3.2.1. RS and WS

Figure 10 depicts how RS and WS affect the UTS of friction stir welded joints with a TA of 1.5°. Maximum joint efficiency is 450 MPa (90%) with low RS and moderate WS measured as the joint's UTS divided by the parent metal's UTS.
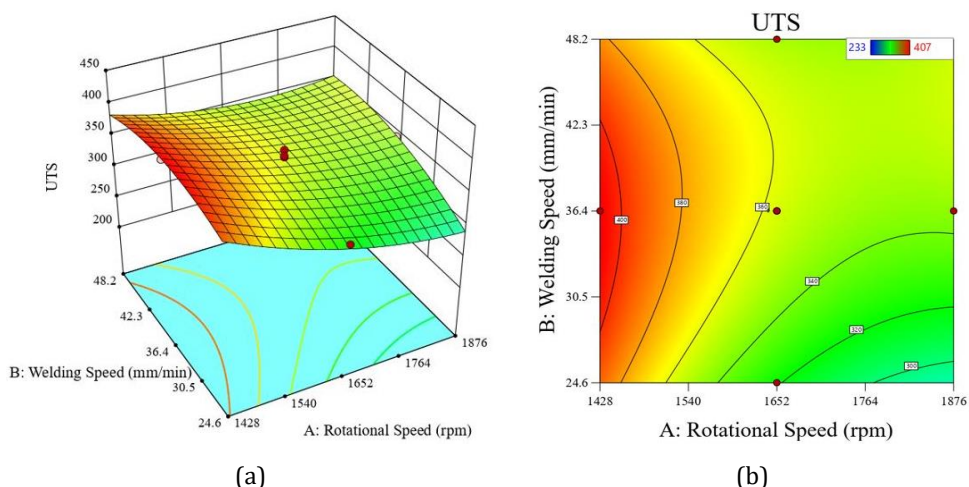

(a)   (b)

Fig.e 10. (a) Three-dimensional response and (b) contour plot for UTS

The heat cycle in FS-welding processes is greatly influenced by RS and WS. Changes in both parameters cause the heat intake to rise, which causes the cooling rate to fall. Joint strength for heat-treatable alloys depends on the melting of hardening precipitates [25]. Solid-state diffusion, that is dependent on temperature and time, is the basis for this dissolution procedure. The solid-state diffusion process takes less time with increased WS and heat input. While the area with joint efficiency greater than 85% is significantly larger the region with joint efficiency exceeding the parent metal is very tiny. A minimum area is one whose joint efficiency is less than 85%. Joint efficiency of more than 80% can be attained at all RS as illustrated in Figure 10(b) provided that the WS is properly selected.

UTS levels below 300 MPa are produced by the procedure when RS is high and WS is low as shown in Figure 10(b). Overheating slows down cooling, extending the holding period required for metallurgical changes. Therefore, RS should be decreased and WS should be moderate in order to get better tensile strength values.

$$UTS = +1521.11387 - 1.78461A + 1.52384B + 479.4588C + 0.00671AB + 0.092076AC + 0.000381A^2 - 0.157021B^2 - 202.27273C^2 \tag{3}$$

The coefficients for term A^2 are larger than those for term B^2, showing that RS is of greater importance than WS, and Equation 5 shows the coded factor values of UTS. The interaction between RS and WS is denoted by the word AB. Equation 5 shows that when the RS has been set to a value of "-1" and the WS to level "0", this interaction is helpful in boosting joint strength. Joint efficiency falls off when the WS has been set to a value of "-1" and the RS is at level "1".

3.2.2. RS and Tilt Angle

Figure 11 depicts the effects of TA and RS at a WS of 36.4 mm/min. The procedure's temperature cycle, stirring manage and movement of materials are all considerably influenced by RS and TA. Minimum RS and moderate TA result in maximum joint efficiency. Heat input rises at higher RS causing a material flow to become more turbulent. Additionally, a decreased TA leads in less plunge force being used throughout the procedure. As a result, incorrect material flow and extrusion of material on the outermost layer due to higher speed of rotation and lower TA result in the production of tunnel defects.
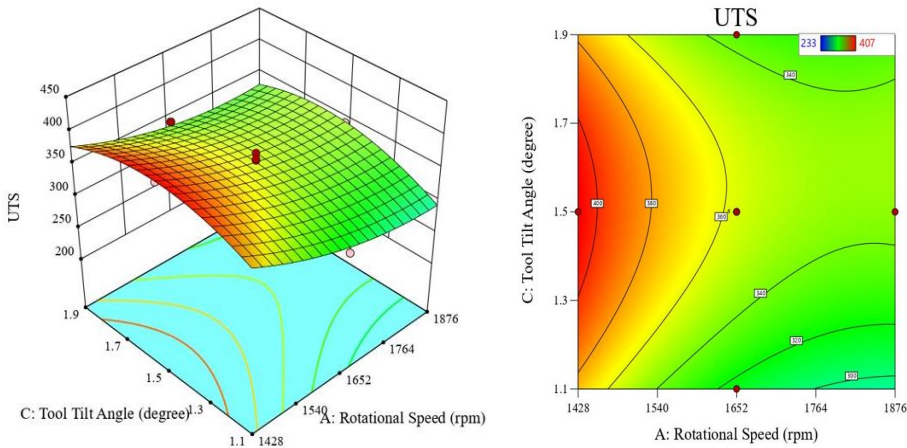

Fig. 11. (a) Three-dimensional response and (b) contour plot for UTS

In the area where the TA fluctuates between 1.3° and 1.7° and the RS varies between 1428 rpm and 1540 rpm, joint efficiency exceeding 86% is attained. Equation 5 shows that RS has a greater impact than TA because the coefficient of A^2 is higher than the coefficient of C^2. The relationship between RS and TA is denoted by the term AC. According to Equation 5 UTS is seen to rise when RS is set to level "-1" and TA is set to level "0". RS at level "1" and WS at level "-1" result in a reduction in joint efficiency.

3.3. Impact of Welding Parameters on EL

The developed design model for EL shows significant first-order and second-order terms, while the interaction between process parameters is insignificant. The design model includes square terms, resulting in curvature plots as shown in Figure 12. Figure 12(a) shows a dramatic decrease in EL as RS rises, which is ascribed to material flow turbulence at faster speeds which causes tunnel defect development in the NZ. In contrast as shown in Figure 12(b) EL steadily rises with WS up to 36.4 mm/min because there is less heat input and less precipitation disintegration. Above 36.4 mm/min EL declines as a result of a greater WS which results in irregular material flow, inadequate heat input, incorrect mixing and cavity development. The effect of TA on EL is shown in Figure 12(c) where EL increases gradually up to 1.5° before declining. This indicates that the tool loses its ability

to effectively manage and keep molten metal under the shoulder above a particular TA limit. Improper stirring causes material to move incorrectly, extrude as flashes onto the working surface and diminish EL.
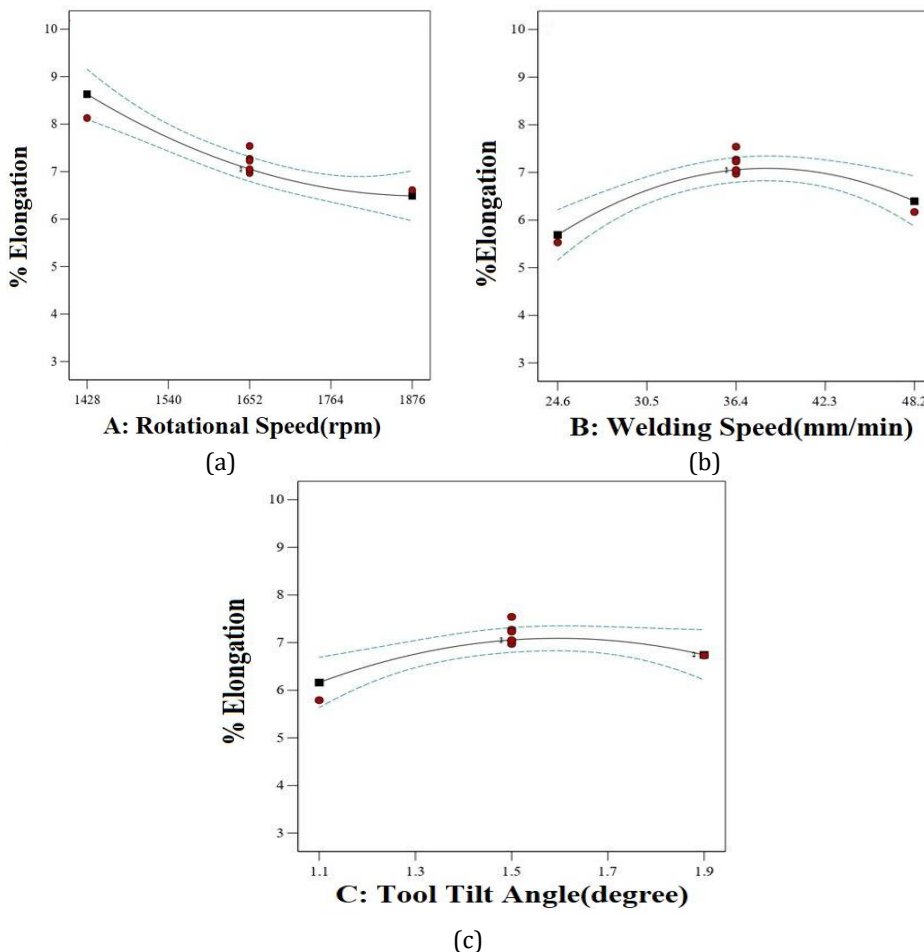

(a)

(b)

(c)

Fig. 12. Performance of overall factors in EL Rotation speed vs EL (a) rotation speed vs UTS, (b) WS vs UTS and (c) tool TA vs UTS

4. Microstructure Analysis

Microstructure analysis was conducted to examine the morphology of the FS weld with maximum strength obtained in experiment no. 15 at (1428rpm,36.4mm/min,1.5°) , medium strength ibtained in experiment no. 3 at (1652rpm, 24.6mm/min,1.5°) lowest strength obtained at experiment no. 4 at (1876rpm,24.6mm/min,1.1°). The microstructure revealed the presence of three distinct zones, including the NZ , TMAZ , and HAZ [2] as shown in Figure 13. In contrast to the FS-welding procedure, it was discovered that the parent metal (PM) had huge, elongated grains. In contrast to TMAZ and HAZ, dynamic recrystallization in the NZ during FS-welding led to the development of fine equiaxed grains [36–37]. Material strengthening is due to the combined effect of dislocations multiplication, secondary phases and the development of finer grains when the density of dislocations reaches a critical value. Furthermore, the HAZ's grains resembled those of the

parent metal since it was heated without undergoing any plastic deformation. Because of mechanical deformation in the TMAZ, the zone's grain sizes were smaller than those of the HAZ Lowest strength. The microstructural study provided insightful information about the structure of the FS weld and the effect of FS welding on the welded joint's microstructure.
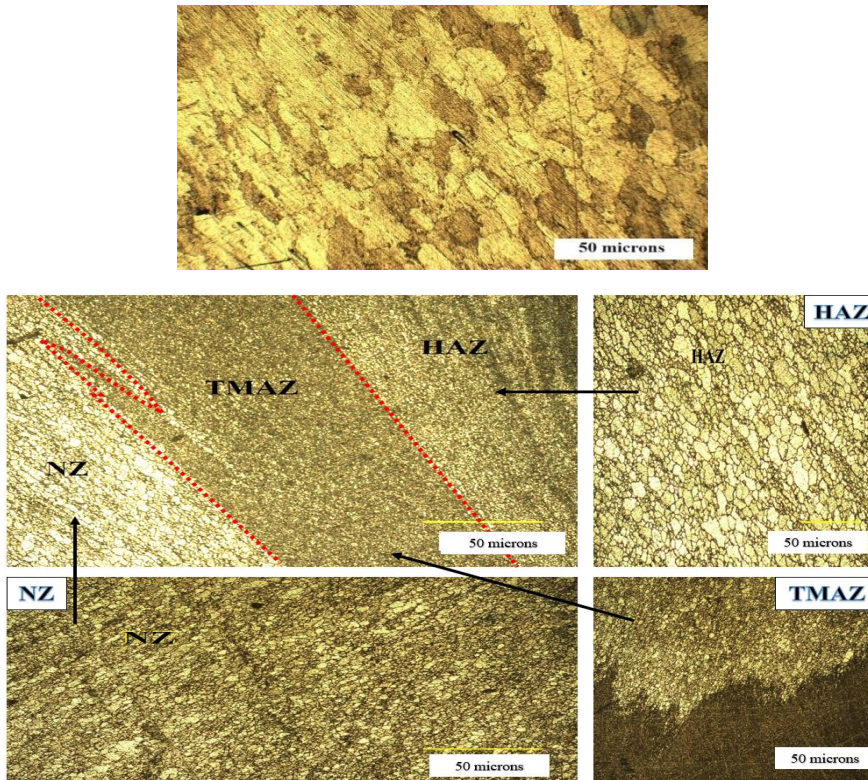

Fig. 13.Microstructural morphology of FS-welding joint

5. Microhardness Distribution

As shown in Figure 14, a microhardness test was carried out with an angle of 0.5 mm for each reading in order to explore the NZ. The base metal was found to have a microhardness of 158 HV. The distribution of microhardness with regard to the process parameters is shown in Figure 14. It was discovered that the NZ's microhardness, which ranged from 103 HV to 118 HV, was lower than that of the parent metal. The dislocation density, size of grains, coarsening, and dissolving of second phase particles were blamed for the decline in microhardness in the NZ. In addition to plastic deformation, the heat cycle variation throughout the process has an impact on the dissolving of strengthening precipitates in alloys from the 8xxx series. Figure 14(a) shows that the NZ's microhardness reduced from 118 HV to 103 HV while its RS increased from 1428 rpm to 1876 rpm. In contrast, the NZ's greatest microhardness was discovered at an average WS of 36.4 mm/min, while the NZ's minimum microhardness was discovered at a WS of 24.6 mm/min. These outcomes matched the tensile strength findings shown in Table 5. As seen in Figures 14(a) and 14(b), applied to the advancing side than the retreating side, the degree of microhardness on the the strengthening precipitates were more easily dissolved as a result of the increased heat input brought on by an increase the rotational speed and a decrease Welding Speed. This

16

resulted in reduced microhardness in the NZ. Of all the constructed joints on the RS, the TMAZ had the highest microhardness. This was due to decreased second phase particle coarsening and dissolution which Sharma et al. [38] also reported. Because more heat was advancing side was lower [39]. This led to the discovery of an asymmetrical microhardness gradient on either side of the centerline. When FS-welding AA7075 Evik et al. [28] noted the similar asymmetrical microhardness distribution. The TMAZ received more intense temperatures than the HAZ, which led to a greater quantity of the second phase particles dissolving, and was therefore determined to have a higher microhardness than the NZ and HAZ. The formation of new nuclei during the process' natural aging can be aided by the breakdown of strengthening precipitates, and the work-hardening effect may also be a factor in the TMAZ's increased microhardness.
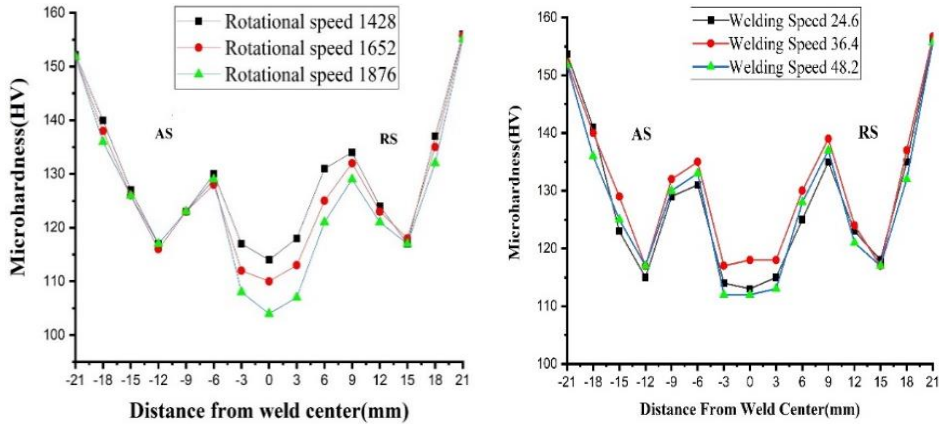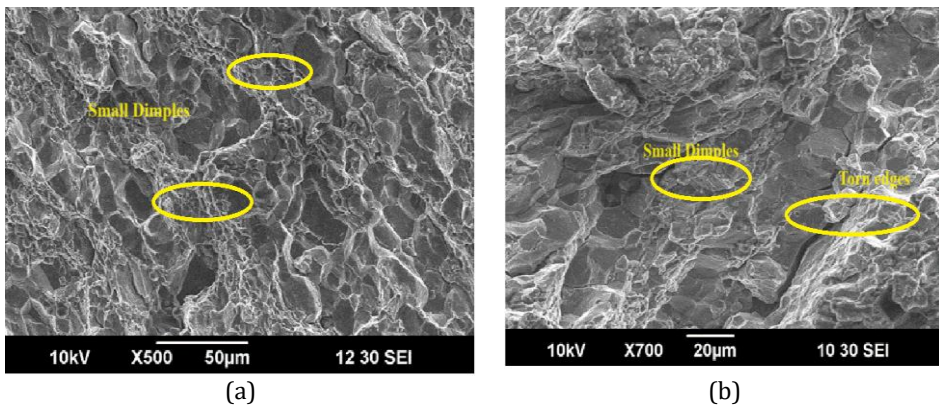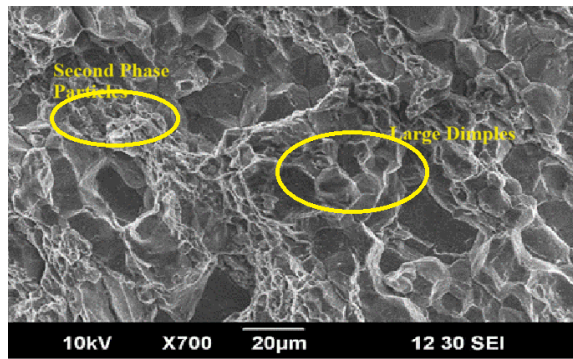

Fig. 14.Microhardness Profile at different a) RS and b) WS

6. Fractography Analysis

As shown in Figure 15 the fractured area of the parent metal, the high strength and the low strength specimens were examined using the fractography analysis. According to the macro fracture the entire artificial joint was shear cracked at an angle of 45 degrees to the tensile axis.

(a)   (b)

(c)

Fig. 15. (a) Tensile specimens of the parent metal (b) the highest strength specimen and (c) the lowest strength specimen

On the surfaces of the parent metal and the manufactured joint tiny and big dimples were visible indicating ductile fracture. Small, deep dimples with ripped edges could be seen on the fracture surface of the specimen with lower tensile strength which suggests reduced ductility. The fracture surface of the joint with higher tensile strength on the other hand revealed wider and shallower dimples, indicating adequate material mixing and greater plastic deformation throughout the process without any flaws. Similar to how the parent metal's fracture surface showed huge dimples which suggested excellent ductility.

6.1 Analysis of Fracture Location

Figure 16 show the failure locations of the fractured aluminium joints. The table shows that the fractured phenomena are observed in different area of welded portion nugget zone, thermos-mechanically heat effected zone and heat affected zone. Mostly failure of FSW joints in the NZ is a common phenomenon.
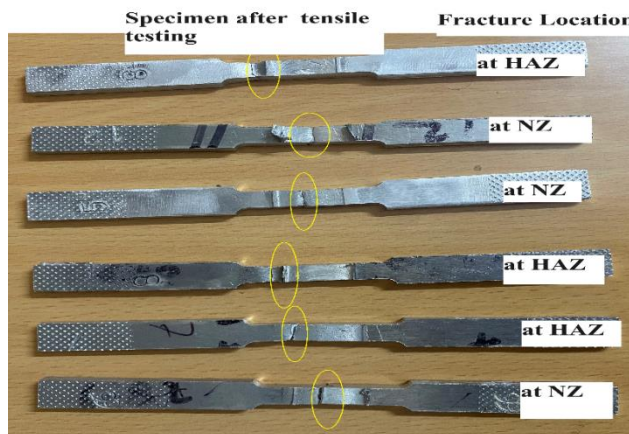

Fig. 16. Tensile specimens of welding aluminium alloys and failure locations

In this research found that mostly fractured at NZ, and others are HAZ. Moreover, it has been shown that HAZ fracture tends to occur on the side of relatively softer materials. The reason is grain coarsening at HAZ as a consequence of high temperature transmission throughout the process. For better understanding SEM is used for fracture failure.

7. Optimization

7.1. Numerical optimization

UTS and EL are the quantitative parameters used in this study to evaluate the efficiency of the FS-welding procedure. The lowest RS, moderate WS and TA together with the maximum UTS are obtained. UTS and % EL are reduced when RS, TA and WS are increased. Higher values in both replies can only be attained with optimal process settings. The ideal UTS and % EL process parameters are chosen using the desirability function.

Harrington first proposed the desirability function approach in 1965 [31–33] and Derinder and Suich later modified it in 1980 [34]. There are several different desirability functions such as target, smaller-the-better and larger-the-better. Equation 3 specifies that the larger-the-better functional is applied to both replies in the current investigation. To calculate the combined desirability function, use equation 4.

$$d_i = \begin{cases} 0 & y_i \leq y_{i*} \\ \left[\dfrac{y_i - y_{i*}}{y_i' - y_{i*}}\right]^t, & y_{i*} < y_i < y_i' \\ 1, & y_i \geq y_i' \end{cases} \tag{4}$$

$$D = (d_1 x d_2 x d_3 \dots x d_m)^{\frac{1}{m}} \tag{5}$$

$$D = (d_1^{w1} x d_2^{w2} x d_3^{w3} x \dots x d_n^{wm})^{1/m} \tag{6}$$

Deringer added weight values to the results in 1994, as shown in Equation 6, to further express the desirability function. Where w is the weight given to the m-th response, m is the overall amount of options, and D stands for the combined desirability. Desirability scales from 0 to 1. Response are less capable as desirability values get closer to 0, whereas Response are more capable as desirability values get closer to 1.

Table 11. Range of input parameters and responses for desirability

Name	Goal	Lower Limit	Upper Limit	Importance
A:Rotational Speed	is in range	1428	1876	3
B:Welding Speed	is in range	24.6	48.2	3
C:Tilt Angle	is in range	1.1	1.9	3
UTS	Maximize	233	407	3
% elongation	Maximize	3.41	8.13	3

Table 12: FS-welding process parameters for highest desirability value

No.	RS	WS	TA	UTS	% Elongation	Desirability
1	1430.477	36.194	1.510	407.488	8.607	1.000
2	1428.036	37.199	1.467	407.466	8.624	1.000
3	1428.000	36.400	1.500	408.182	8.631	1.000
4	1430.120	36.423	1.507	407.534	8.611	1.000
5	1428.676	36.410	1.492	407.919	8.625	1.000

The current study's goal is to determine the ideal input parameter values for the FS-welding process in order to maximize desirability [35]. Table 11 lists the limited values of the process parameters used in this study and describes the ideal values at which the highest level of desirability is attained. The overall desirability plot for both the individual

and combined process variables is shown in Figure 17. The ramp function's plots in Figure 18 show the values of the process variables needed to achieve high desirability.
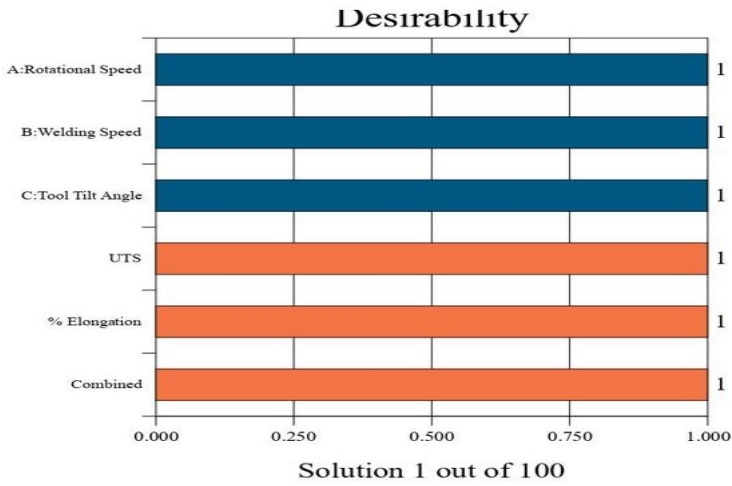

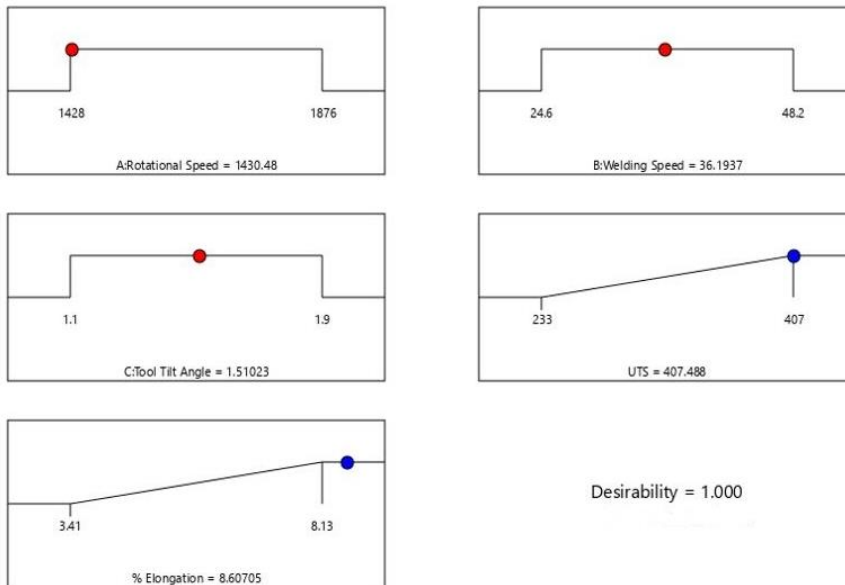Fig.17. Desirability of process variables and outcomes overall

Fig. 18. Ramp diagram of optimized input and output responses of JOINTS

Table 13. Confirmation experiments result

RS (rpm)	WS (mm/min)	TA (degree)	UTS (MPa) Predicted	UTS (MPa) Actual	EL Predicted	EL actual
1430.47	36.19	1.51	407.48	407	8.60	8.13

As shown in Figure 19, the desirable index of 1 was attained at the ideal process settings. The WS and TA exhibited negative effects before and after 36.91mm/min and 1.51°respectively while the decrease in RS had a beneficial impact on the desirability function. The multi-response optimization's greatest desirability function values were attained at RS 1430.47 rpm, TA 1.51° and WS 36.19 mm/min table13. presents the findings of the validation experiment carried out to establish the ideal circumstance for maximal desirability. The experimental results were in line with what was expected.
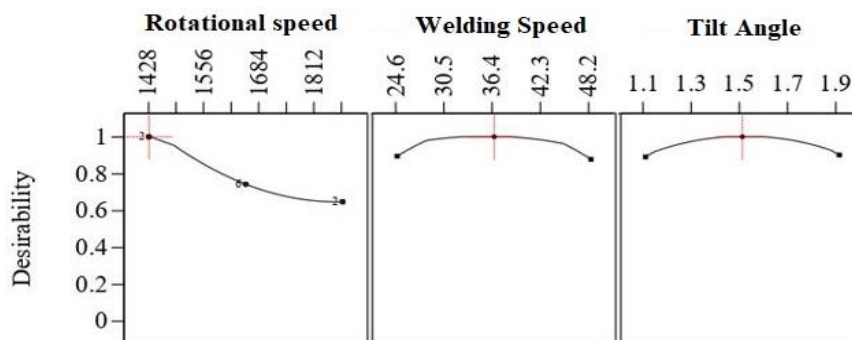

Fig. 19. Overall desirability curve for process parameters

8. Conclusion

The statistical design models for UTS and EL in the current study were created using CCD-RSM. It was discovered that CCD-RSM was used to create these models, which were shown to be substantial and quadratic in nature. According to the regression design models, RS (rotational speed) was the most important variable for both responses and each input variable was thought to be the least effective parameter. This was the case even though RS was not the sole factor that was taken into account. All components, with the exception of WS and TA were found to interact significantly for UTS, but there was no proof that this interaction was substantial for EL. The maximum joint strength that could be achieved was 407 MPa. The maximum joint strength was found where RS was least and WS was medium level in the 3D interaction plot of RS and WS for UTS, which can be attributed to sufficient heat input during the process. The fact that this location was situated in the middle of the plot provided additional support for this conclusion. The 3D interaction plot between RS and TA for UTS similarly showed that the region where RS was reduced to its lower limit while TA was modest was where the best joint strength was reached. For the UTS, this was true. We were able to get the perfect conditions for achieving the maximum UTS and EL at an RS of 1430.47 rpm, WS of 36.19 mm/min and a TA (tilt angle) of 1.51°. The maximum EL of 10.57% that we were able to get was higher than that of the parent metal. The grains in the parent metal and the HAZ were found to be relatively big and elongated, whereas the grains in the NZ were found to be fine due to mechanical stirring. The microhardness of the TMAZ was discovered to be higher than typical due to the intense heat. This resulted in more second phase particles dissolving, which could result in the production of additional nuclei during the subsequent natural aging process. Furthermore, it was shown that the increased microhardness in the TMAZ was a result of the work hardening effect. Finally, the presence of dimples on the fracture surfaces of all the samples allowed ductile fracture to be recognized.

References

[1] Yang Y, Zhang J, Li W, Zhuang W, Jiang H, Wu X, et al. Research progress on the microstructure and mechanical properties of friction stir welded Al-Li alloy joints. J Manuf Process. 2022;82(May):230-44. https://doi.org/10.1016/j.jmapro.2022.07.067

[2] Seetharaman R, Seeman M, Kanagarajan D, Sivaraj P, Saravanan I. A statistical evaluation of the corrosion behaviour of friction stir welded AA2024 aluminium alloy. Mater Today Proc. 2020;22:673-80. https://doi.org/10.1016/j.matpr.2019.09.066

[3] Nosrati HG, Yazdani NM, Khoran M. Double-sided friction stir welding of AA 2024-T6 joints: Mathematical design modeling and optimization. CIRP J Manuf Sci Technol. 2022;36(2022):1-11. https://doi.org/10.1016/j.cirpj.2021.10.010

[4] Palanivel R, Mathews PK, Murugan N, Dinaharan I. Prediction and optimization of wear resistance of friction stir welded dissimilar aluminum alloy. Procedia Eng. 2012;38:578-84. https://doi.org/10.1016/j.proeng.2012.06.072

[5] Elatharasan G, Kumar VSS. An experimental analysis and optimization of process parameter on friction stir welding of AA 6061-T6 aluminum alloy using RSM. Procedia Eng. 2013;64:1227-34. https://doi.org/10.1016/j.proeng.2013.09.202

[6] Rambabu G, Naik DB, Rao CHV, Rao KS, Reddy GM. Optimization of friction stir welding parameters for improved corrosion resistance of AA2219 aluminum alloy joints. Def Technol. 2015;11(4):330-7. https://doi.org/10.1016/j.dt.2015.05.003

[7] Elatharasan G, Kumar VSS. Modelling and optimization of friction stir welding parameters for dissimilar aluminium alloys using RSM. Procedia Eng. 2012;38:3477-81. https://doi.org/10.1016/j.proeng.2012.06.401

[8] Bruce AR, Kumar PP, Arul K, Kumar PM, Kumar SL, Aravindh. Experimental characteristics and optimization of friction stir welded AA5052-AA6061 using RSM technique. Mater Today Proc. 2022;59:1379-87. https://doi.org/10.1016/j.matpr.2021.12.099

[9] Qin Q, Zhao H, Li J, Zhang Y, Su X. Microstructure and mechanical properties of friction stir processed Al–Mg2Si alloys. Trans Nonferrous Met Soc China. 2020;30(9):2355-68. https://doi.org/10.1016/S1003-6326(20)65384-5

[10] Liu Z, Zhang H, Hou Z, Feng H, Dong P, Liaw PK. Microstructural origins of mechanical and electrochemical heterogeneities of friction stir welded heat-treatable aluminum alloy. Mater Today Commun. 2020;24(May):101229. https://doi.org/10.1016/j.mtcomm.2020.101229

[11] Sharma HK, Bhatt K, Shah K, Joshi U. Experimental analysis of friction stir welding of dissimilar alloys AA6061 and Mg AZ31 using circular butt joint geometry. Procedia Technol. 2016;23:566-72. https://doi.org/10.1016/j.protcy.2016.03.064

[12] Özel C. Research of production times and cutting of the spur gears by end mill in CNC milling machine. Int J Adv Manuf Technol. 2011;54(1-4):203-13. https://doi.org/10.1007/s00170-010-2943-5

[13] Mahto RP, Bhoje R, Pal SK, Joshi HS, Das S. A study on mechanical properties in friction stir lap welding of AA 6061-T6 and AISI 304. Mater Sci Eng A. 2016;652:136-44. https://doi.org/10.1016/j.msea.2015.11.064

[14] Verma S, Misra JP. Experimental investigation on friction stir welding of dissimilar aluminium alloys. Proc Inst Mech Eng Part E J Process Mech Eng. 2021;235(5):1545-54. https://doi.org/10.1177/09544089211008694

[15] Verma S, Meenu, Misra JP. Study on temperature distribution during friction stir welding of 6082 aluminum alloy. Mater Today Proc. 2017;4(2):1350-6. https://doi.org/10.1016/j.matpr.2017.01.156

[16] Verma S, Misra JP, Gupta M. Study of temperature distribution and parametric optimization during FS-welding of AA6082 using statistical approaches. SAE Int J Mater Manuf. 2019;12(1):73-82. https://doi.org/10.4271/05-12-01-0005

[17] Verma S, Gupta M, Misra JP. Effect of pin-profiles on thermal cycle, mechanical and metallurgical properties of friction stir-welded aviation-grade aluminum alloy. Proc Inst Mech Eng Part B J Eng Manuf. 2019;233(11):2183-95. https://doi.org/10.1177/0954405419832109

[18] Verma S, Gupta M, Misra JP. Effect of preheating and water cooling on the performance of friction-stir-welded aviation-grade aluminum alloy joints. J Mater Eng Perform. 2019;28(7):4209-20. https://doi.org/10.1007/s11665-019-04183-z

[19] Verma S, Gupta M, Misra JP. Study of thermal cycle, mechanical, and metallurgical properties of friction stir welded aviation grade aluminum alloy. Proc Inst Mech Eng Part:G J.Aerosp Eng. 2019;233(11):4202-13. https://doi.org/10.1177/0954410018816601

[20] Verma S, Misra JP, Gupta M. Procedure to find out the optimal ranges of process parameters for friction stir welding. Proc Inst Mech Eng Part L J Mater Des Appl. 2021;235(5):1172-80. https://doi.org/10.1177/1464420721993145

[21] Mahto RP, Kumar R, Pal SK, Panda SK. A comprehensive study on force, temperature, mechanical properties and micro-structural characterizations in friction stir lap welding of dissimilar materials (AA6061-T6 & AISI304). J Manuf Process. 2018;31:624-39. https://doi.org/10.1016/j.jmapro.2017.12.017

[22] Raja R, Parthiban A, Jeyakumar S, Radha Krishnan B. Investigation of mechanical properties of friction stir welding aluminium alloy AA7475-T651 and AA2219-O. Mater Today Proc. 2022;60:1421-3. https://doi.org/10.1016/j.matpr.2021.10.439

[23] Rajendran C, Srinivasan K, Balasubramanian V, Balaji H, Selvaraj P. Effect of tool TA on strength and microstructural characteristics of friction stir welded lap joints of AA2014-T6 aluminum alloy. Trans Nonferrous Met Soc China. 2019;29(9):1824-35. https://doi.org/10.1016/S1003-6326(19)65090-9

[24] RajKumar V, VenkateshKannan M, Sadeesh P, Arivazhagan N, Devendranath Ramkumar K. Studies on effect of tool design and welding parameters on the friction stir welding of dissimilar aluminium alloys AA 5052 - AA 6061. Procedia Eng. 2014;75:93-7. https://doi.org/10.1016/j.proeng.2013.11.019

[25] Mehta KP, Badheka VJ. Effects of tool pin design on formation of defects in dissimilar friction stir welding. Procedia Technol. 2016;23:513-8. https://doi.org/10.1016/j.protcy.2016.03.057

[26] Mehta KP, Badheka VJ. Influence of tool pin design on properties of dissimilar copper to aluminum friction stir welding. Trans Nonferrous Met Soc China. 2017;27(1):36-54. https://doi.org/10.1016/S1003-6326(17)60005-0

[27] Boldsaikhan E, Corwin E, Logar A, Arbegast W. Neural network evaluation of weld quality using FS-welding feedback data. 2006.

[28] Fratini L, Buffa G, Palmeri D. Using a neural network for predicting the average grain size in friction stir welding processes. Comput Struct. 2009;87:1166-74. https://doi.org/10.1016/j.compstruc.2009.04.008

[29] Ghetiya ND, Patel KM. Prediction of wear behaviour and optimization of process parameters of AA7075-T6 hybrid composite using Taguchi coupled ANN approach. Measurement. 2018;127:185-97.

[30] Wakchaure KN, Thakur AG, Gadakh V, Kumar A. Multi-Objective Optimization of Friction Stir Welding of Aluminium Alloy 6082-T6 Using Hybrid Taguchi-Grey Relation Analysis-ANN Method. Mater Today Proc. 2018;5(2):7150-9. https://doi.org/10.1016/j.matpr.2017.11.380

[31] Alkayem NF, Parida B, Pal S. Optimization of friction stir welding process parameters using soft computing techniques. Soft Comput. 2017;21(23):7083-98. https://doi.org/10.1007/s00500-016-2251-6

[32] Babu KK, Rao CR, Reddy GM, et al. Parameter optimization of friction stir welding of cryorolled AA2219 alloy using artificial neural network design modeling with genetic

algorithm. Int J Adv Manuf Technol. 2018;94(9-12):3117-29. https://doi.org/10.1007/s00170-017-0897-6

[33] Masoudi Nejad R, Sina N, Ghahremani Moghadam D, Branco R, Macek W, Berto F. Artificial neural network based fatigue life assessment of friction stir welding AA2024-T351 aluminum alloy and multi-objective optimization of welding parameters. Int J Fatigue. 2022;160:106840. https://doi.org/10.1016/j.ijfatigue.2022.106840

[34] Prasanna P, Penchalayya CH, Rao DA. Effect of tool pin profiles and heat treatment process in the friction stir welding of AA 6061 aluminium alloy. Am J Eng Res. 2013;2(1):7-15.

[35] Haribalaji V, Sampath, Asif MM. Optimization of friction stir welding process to join dissimilar AA2014 and AA7075 aluminum alloys. Mater Today Proc. 2021;50:2227-34. https://doi.org/10.1016/j.matpr.2021.09.499

[36] Nait Salah A, Mehdi H, Mehmood A, Hashmi AW, Malla C, Kumar R. Optimization of process parameters of friction stir welded joints of dissimilar aluminum alloys AA3003 and AA6061 by RSM. Mater Today Proc. 2022;56:1675-83. https://doi.org/10.1016/j.matpr.2021.10.288

[37] Sarvaiya J, Singh D. Selection of the optimal process parameters in friction stir welding/processing using particle swarm optimization algorithm. Mater Today Proc. 2022;62:896-901. https://doi.org/10.1016/j.matpr.2022.04.062

[38] Simoncini M, Forcellese A, Mancini E, Chiappini G, Sasso M. Experimental and numerical investigation on forming limit curves of AA6082 aluminum alloy at high strain rates. Int J Adv Manuf Technol. 2021;112(7-8):1973-91. https://doi.org/10.1007/s00170-020-06448-7

[39] Abd Elnabi MM, Elshalakany AB, Abdel-Mottaleb MM, Osman TA, El Mokadem A. Influence of friction stir welding parameters on metallurgical and mechanical properties of dissimilar AA5454-AA7075 aluminum alloys. J Mater Res Technol. 2019;8(2):1684-93. https://doi.org/10.1016/j.jmrt.2018.10.015

[40] Subramanian M, Sathishkumar N, Sasthrigal JS, Arunkumar N, Hariharan V. Optimization of process parameters in friction stir welded dissimilar magnesium alloys using RSM. Mater Today Proc. 2019;46:9736-46. https://doi.org/10.1016/j.matpr.2020.09.049

[41] Khan N. Optimization of friction stir welding of AA6062-T6 alloy. Mater Today Proc. 2018;29:448-55. https://doi.org/10.1016/j.matpr.2020.07.298

[42] Haribalaji V, Boopathi S, Asif MM. Optimization of friction stir welding process to join dissimilar AA2014 and AA7075 aluminum alloys. Mater Today Proc. 2021;50:2227-34. https://doi.org/10.1016/j.matpr.2021.09.499

[43] Kumar SR, Rao VS, Pranesh RV. Effect of Welding Parameters on Macro and Microstructure of Friction Stir Welded Dissimilar Butt Joints between AA7075-T651 and AA6061-T651 Alloys. Procedia Mater Sci. 2014;5:1726-35. https://doi.org/10.1016/j.mspro.2014.07.362

[44] Heirani F, Abbasi A, Ardestani M. Effects of processing parameters on microstructure and mechanical behaviors of underwater friction stir welding of Al5083 alloy. J Manuf Process. 2017;25:77-84. https://doi.org/10.1016/j.jmapro.2016.11.002